Journal of Hazardous Materials 424 (2022) 127563

Contents lists available at ScienceDirect

Journal of Hazardous Materials

journal homepage: www.elsevier.com/locate/jhazmat

Research Paper

Visible light photocatalytic degradation of sulfanilamide enhanced by Mo doping of BiOBr nanoflowers

Yunyun Wu [a,1], Haodong Ji [b,1], Qiming Liu [c], Zhaoyang Sun [d], Peisheng Li [b], Peiren Ding [a], Ming Guo [a], Xiaohong Yi [e], Wenlu Xu [a], Chong-Chen Wang [e,*], Shuai Gao [a], Qiang Wang [a,*], Wen Liu [b], Shaowei Chen [c,*]

[a] Laboratory for Micro-sized Functional Materials & College of Elementary Education and Department of Chemistry, Capital Normal University, Beijing 100048, PR China
[b] Beijing Innovation Center for Engineering Science and Advanced Technology (BIC-ESAT) and Key Laboratory of Water and Sediment Sciences, Ministry of Education, College of Environmental Sciences and Engineering, Peking University, Beijing 100871, PR China
[c] Department of Chemistry and Biochemistry, University of California, 1156 High Street, Santa Cruz, CA 95064, USA
[d] Office of Forensic Medicine and Toxicology, Department of Criminal Science and Technology, Beijing People's Police College, Beijing 102202, PR China
[e] Beijing Key Laboratory of Functional Materials for Building Structure and Environment Remediation, Beijing University of Civil Engineering and Architecture, Beijing 100044, PR China

ARTICLE INFO

Editor: Dr. R. Debora

Keywords:
Mo-doped BiOBr
Band gap
Photocatalytic
Visible light
Degradation
Sulfanilamide

ABSTRACT

Design of high-efficiency visible light photocatalysts is critical in the degradation of antibiotic pollutants in water, a key step towards environmental remediation. In the present study, Mo-doped BiOBr nanocomposites are prepared hydrothermally at different feed ratios, and display remarkable visible light photocatalytic activity towards the degradation of sulfanilamide, a common antibacterial drug. Among the series, the sample with 2% Mo dopants exhibits the best photocatalytic activity, with a performance 2.3 times better that of undoped BiOBr. This is attributed to Mo doping that narrows the band gap of BiOBr and enhances absorption in the visible region. Additional contributions arise from the unique materials morphology, where the highly exposed (102) crystal planes enrich the photocatalytic active sites, and facilitate the adsorption of sulfanilamide molecules and their eventual attack by free radicals. The reaction mechanism and pathways are then unraveled based on theoretical calculations of the Fukui index and liquid chromatography/mass spectrometry measurements of the reaction intermediates and products. Results from this study indicate that deliberate structural engineering based on heteroatom doping and morphological control may serve as an effective strategy in the design of highly active photocatalysts towards antibiotic degradation.

1. Introduction

Antibiotics are a kind of drugs with strong bactericidal effects (S. Li et al., 2021; M. Li et al., 2021; W. Li et al., 2021; Wang et al., 2020), and have been widely used in hospitals, farms, and animal husbandries (Qin et al., 2021; Liu et al., 2020; Wang et al., 2020). Such extensive uses of antibiotics have been known to cause the residues to enter the environment along with industrial wastewater and human and animal excrement, which poses an unpredictable impact on the ecosystem and human health (B. Li et al., 2019; H. Li et al., 2019; P. Li et al., 2019), such as the formation of antibiotic-resistant genes (Du et al., 2020; Hamiwe et al., 2019). Sulfanilamide is a common antibacterial drug used in clinical treatment (Wang et al., 2019), and residues of sulfanilamide have been found in feces, soil and surface water (Zhu et al., 2016). Although the residue concentration in the aquatic environment is usually low, the long-term existence can increase the resistance of microorganisms, and reduce the body's immunity, resulting in potential threat to human health (Senasu et al., 2021a, 2021b; J. Wang et al., 2020; Y. Wang et al., 2020). Thus, it is of both fundamental and technological significance to develop effective technologies to remove antibiotic residues from environmental water (Liu et al., 2021; Younis et al., 2021; Senasu et al., 2021a, 2021b).

* Corresponding authors.
E-mail addresses: wangchongchen@bucea.edu.cn (C.-C. Wang), qwchem@gmail.com (Q. Wang), shaowei@ucsc.edu (S. Chen).
[1] These authors contributed equally to this work.

https://doi.org/10.1016/j.jhazmat.2021.127563
Received 4 September 2021; Received in revised form 11 October 2021; Accepted 18 October 2021
Available online 24 October 2021

Up to now, a variety of methods have been examined to remove sulfanilamide from environmental water, such as biodegradation, chemisorption and membrane technology. However, due to the low elimination rate of sulfanilamide (thanks to its relatively stable chemical structure) and/or the unsatisfactory degradation activity of these traditional technologies, their practical applications have remained limited (Adamek et al., 2012). Photocatalysis has great prospects in the removal of antibiotics from environmental water and sterilization, due to its advantages of high efficiency, economic viability, and green nature (Han et al., 2021). A range of semiconductor materials have been used as photocatalysts, such as carbon nanotubes (Khan et al., 2021), metal sulfides (Niu et al., 2020), and metal oxides (Qin et al., 2021). Among these, BiOBr is a unique photocatalyst that features a special layered structure composed of $[Bi_2O_2]^{2+}$ layers sandwiched between two $[Br_2]^{2-}$ layers, where the interlayer electrostatic field greatly promotes the separation and transport of photoexcitons, leading to improved photocatalytic activity (Wang and Zhuan, 2020; Wang et al., 2020; Senasu et al., 2021a, 2021b). Yet, with a rather large band gap (ca. 2.9 eV), pristine BiOBr shows only limited absorption in the visible range, poor electron transport capacity, and a low number of active sites. Further structural engineering of BiOBr is needed to achieve visible-light photo absorption and enhance the photocatalytic performance. Currently, the commonly used strategies include construction of heterojunctions, defect engineering and elemental doping. Table S1 lists the application of BiOBr nanocomposites synthesized through different strategies in the photocatalytic degradation of antibiotics in recent years.

Among the various modification approaches, doping is a simple and effective strategy, which can easily adjust the electronic structure and form new energy levels but without changing the main crystal structure (Qiao et al., 2020). In fact, metal ion doping has been exploited extensively as an engineering method to reduce the materials band gap and extend the absorption to the visible range, leading to enhanced separation of photocarriers and ultimately photocatalytic performance (Wang et al., 2017). For instance, transition metals have been successfully doped into BiOBr for effective visible light fixation of N_2 and degradation of organic pollutants (Y. Chen et al., 2021; X. Chen et al., 2021; Qu et al., 2021). Molybdenum (Mo) is a transition metal with its outer orbitals semi-filled with six electrons. As the ionic radius of Mo (0.54 Å) is much smaller than that of Bi (1.03 Å), Mo elements can be readily doped into the lattice of BiOBr to engineer the band structure (Tayebi et al., 2019). Inspired by these earlier results, in the present study Mo-doped BiOBr was prepared and used for the first time to improve the visible-light photocatalytic degradation of sulfanilamide. Note that in comparison with other antibiotics, sulfanilamide is relatively stable with a sulfonamide functional group and aniline ring in the molecular structure (Ghahremani et al., 2017). Thus, it remains a challenge to efficiently remove sulfanilamide residuals from environmental water (Wang et al., 2019; Dong et al., 2016).

The synthesis of BiOBr nanocomposites includes co-precipitation, chemical exfoliation, template-assisted, sol-gel and hydrothermal methods. The hydrothermal method is considered to be the most suitable method for preparing composite materials due to its advantages of environmental friendliness, ease of operation, and low cost (Hunge et al., 2021). Moreover, the size, distribution, and morphology of particles can be improved by changing the hydrothermal conditions (e.g., reaction temperature, pH, and reaction time) (Sadjid et al., 2019). Herein, Mo-doped BiOBr nanoflowers were synthesized hydrothermally. It was found that the resulting samples displayed a narrowed bandgap, apparent absorption in the visible range, and improved carrier transport. Significantly the photocatalytic performance towards the degradation of sulfanilamide was markedly enhanced, in comparison to that of pristine BiOBr.

Notably, density functional theory (DFT) calculations have been widely used to explore the quantum properties of organic/inorganic molecular structures and evaluate the reaction pathways. For example, Ji et al. (2020, 2021), J. Liu et al. (2019), W. Liu et al. (2019) investigated the potential reactive sites of various organic contaminants, such as sulfamethazine, diclofenac, and ciprofloxacin, according to the Fukui function based on DFT calculations. Therefore, in the present study, the reaction mechanism and pathways were evaluated by theoretical calculations of the Fukui index, where the reaction intermediates and products were quantified by liquid chromatograghy-mass spectrometry (LC-MS) measurements.

2. Experimental section

The details about chemical reagents, instruments for material structural characterization, and theoretical calculations are included in the Supplementary Information.

2.1. Sample preparation

Mo-doped BiOBr nanoflowers were synthesized hydrothermally (Y. Chen et al., 2021; X. Chen et al., 2021). In a typical experiment, two solutions were prepared separately. The first solution included $Bi(NO_3)_3{\cdot}5H_2O$ (1.94 g) and a calculated amount of Na_2MoO_4 (varied from 8.3 to 68.7 mg) in 30 mL of a 1 M HNO_3 solution. The other was 0.476 g of KBr dissolved into a mixture of 25 mL of deionized water and 20 mL of ethylene glycol with the pH set to 7 by $NH_3{\cdot}H_2O$. These two solutions were then mixed and loaded into a 100 mL Teflon-lined stainless-steel autoclave undergoing thermal treatment at 160 °C for 24 h. After being cooled down to ambient temperature, the resulting precipitate was centrifuged, rinsed several times with deionized water and ethanol, desiccated overnight in a vacuum oven, and grounded for further use. These samples were referred to as *x*%Mo-BiOBr, with *x*% being the Mo dopant concentration. As a control, undoped BiOBr was prepared in the same manner but without the addition of Na_2MoO_4.

2.2. Photocatalysis

The photocatalytic activities of undoped and Mo-doped BiOBr nanoflowers were examined by the degradation of sulfanilamide using a 300 W xenon lamp (with a UV cut-off filter, > 420 nm) as the simulated sun light (FX300, Perfect Light). Specifically, 50 mL of a 10 mg L^{-1} sulfanilamide solution, along with 20 mg of the BiOBr or *x*%Mo-BiOBr obtained above, was added into a quartz tube, and an adsorption/desorption equilibrium was reached by continuous stirring of the solution for 30 min in the dark. Degradation was then initiated by photoirradiation of the reaction solution with the xenon lamp. An aliquot (2.0 mL) of the solution was removed from the quartz tube in a time interval of 10 min, and the contained photocatalyst was removed by centrifugation. The maximum absorption of sulfanilamide at 256 nm was measured with a UV–vis spectrophotometer. The initial pH was regulated with HCl (0.1 M) or NaOH (0.2 M) to 3, 5, 6 or 10. Radical formation was examined by electron spin resonance (ESR) measurements with a Bruker ER200-SRC-10/12 spectrometer using 5,5-dimethyl-1-pyrroline-N-oxide (DMPO) as the spin-trapping agent, where $O_2^{\bullet-}$ and •OH were generated and collected in H_2O and methanol, respectively (X. Xu et al., 2021; J. Xu et al., 2021). Photodegradation intermediates and products were quantitatively assessed by LC-MS analysis with a Thermo Scientific Q Exactive/Focus LC–MS/MS/Ultimate 3000 UPLC instrument.

3. Results and discussion

3.1. Characterizations

The sample structures were first analyzed by XRD studies. It can be seen from Fig. 1a that undoped BiOBr exhibited five major diffraction peaks at $2\theta = 10.88°$, 21.84°, 31.68°, 39.32° and 57.16°, due to the (001), (002), (102), (112) and (212) crystal faces of tetragonal BiOBr (JCPDS#09-0393) (Zhang et al., 2014), respectively. Consistent

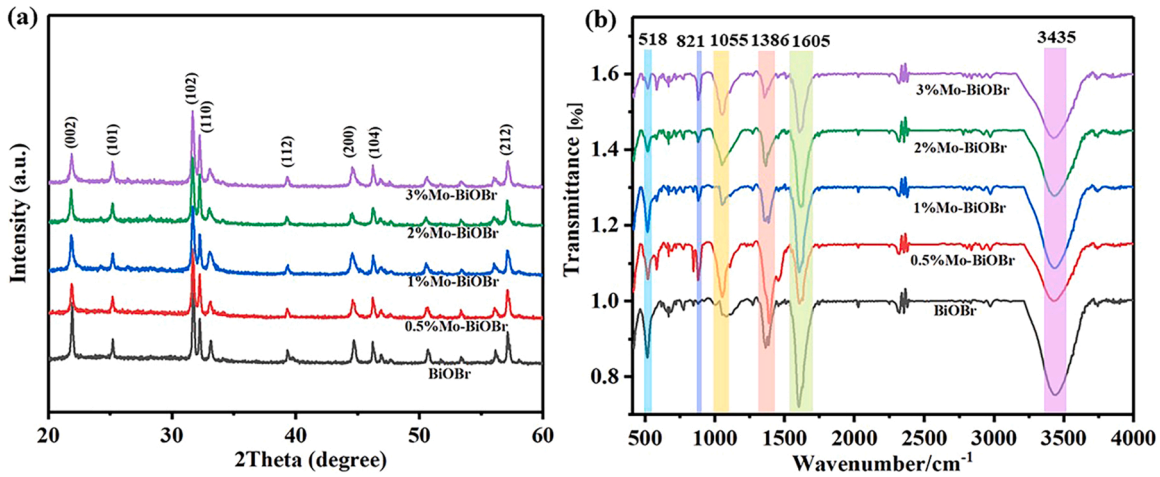

Fig. 1. (a) XRD patterns and (b) FTIR spectra of Mo-doped BiOBr nanocomposites.

diffraction patterns were observed with the Mo-doped BiOBr samples, suggesting that the doping of Mo did not significantly change the crystalline structure of BiOBr (Wu et al., 2016). The corresponding Fourier-transform infrared (FTIR) spectra were shown in Fig. 1b. Again, the doped and undoped samples exhibit very similar profiles, attesting virtually no change of the chemical structure of the sample upon Mo doping (Yan et al., 2018). Several vibrational features can be resolved. The peaks at 3435 and 1605 cm^{-1} can be ascribed to the O-H tensile and bending vibrations of free water (Huang et al., 2020), respectively. The vibrations at 1386 and 518 cm^{-1} are due to the asymmetric Bi-Br stretching and symmetrical stretching of the Bi-O bond in BiOBr (Wu et al., 2020). In contrast to the undoped BiOBr, Mo-doped BiOBr was observed to show additional vibrations at 821 and 1055 cm^{-1}, which can be ascribed to the Bi—O and Mo—O bonds, respectively (Wu et al., 2020; Gupta et al., 2017). The formation of Mo—O bonds indicated that Mo ions were successfully incorporated into the BiOBr lattice replacing part of the Bi ions (Wu et al., 2020).

Scanning electron microscopy (SEM) measurements were then carried out to characterize the morphological details of the undoped and Mo-doped BiOBr composites. Fig. 2a and c and S1 show the SEM images of BiOBr and 2%Mo-BiOBr at low resolution, both of which exhibit a regular and uniform morphology of nanoflowers. From Fig. 2b, the undoped BiOBr can be seen to exhibit a uniformly dispersed sheet-like structure, and such nanosheets were connected to each other forming a porous scaffold. The 2%Mo-BiOBr composite showed a similar structure (Fig. 2d), demonstrating that the introduction of Mo dopants did not induce an appreciable change of the BiOBr morphology, in accord with results from XRD measurements (Fig. 1a).

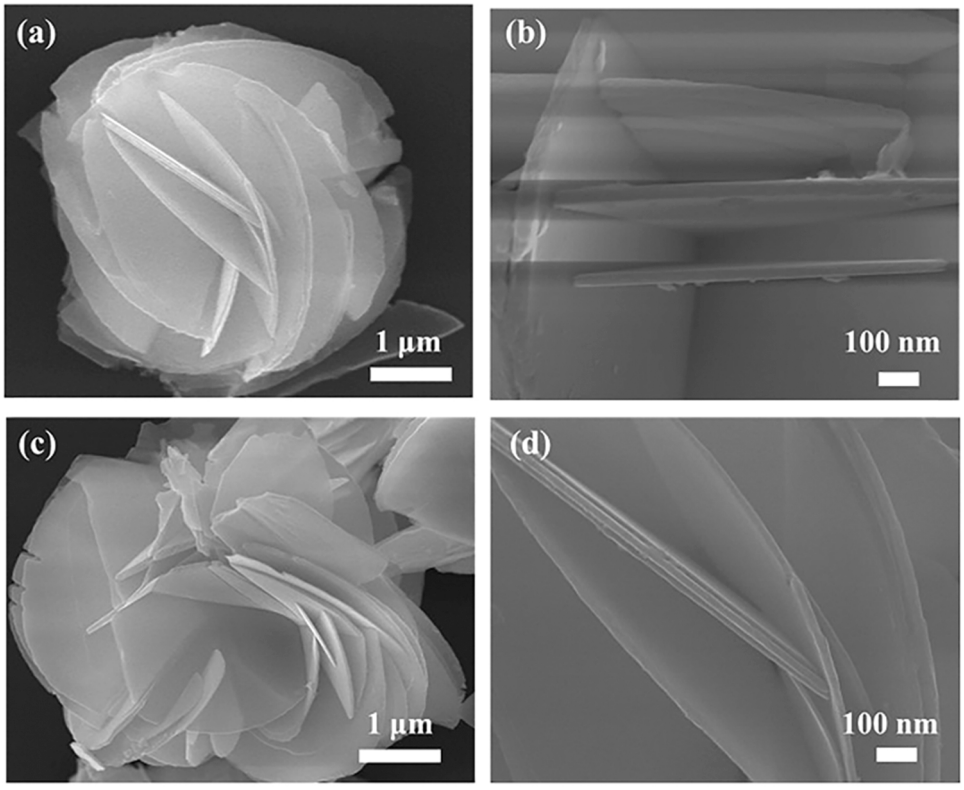

Fig. 2. SEM images of (a and b) undoped BiOBr and (c and d) 2%Mo-BiOBr.

From the EDX profiles in Fig. S2, one can see that the undoped BiOBr sample consisted of only Bi, Br and O with an atomic ratio close to 1:1:1. The 2%Mo-doped BiOBr sample exhibited a similar profile, with the Mo content (2.12%) consistent with the initial feed. These observations suggest high purity of the samples.

The sample microstructures were further examined by transmission electron microscopy (TEM) studies. From Fig. 3a and d, the nanoflowers of undoped BiOBr and 2% Mo-BiOBr can be seen to consist of an assembly of nanosheets. In high-resolution TEM measurements (Fig. 3b and e), one can see that both samples displayed well-defined lattice fringes with an interplanar spacing of 0.173 nm, corresponding to the $(\bar{2}11)$ crystalline planes of tetragonal BiOBr. This indicates dominant exposure of the BiOBr (102) planes (Y. Chen et al., 2021; X. Chen et al., 2021). Fig. 3c and f show the associated selected area electron diffraction (SAED) patterns, where the (102) and (104) diffractions can be readily identified. Furthermore, in elemental mapping analysis (Fig. 3g–l) the elements of Bi, O, Br, and Mo can be seen to exhibit a uniform distribution within the 2%Mo-BiOBr sample, indicating successful and even doping of Mo into the BiOBr lattice (Jiao et al., 2021). These samples also exhibit a similar specific surface area of about 6.43 m^2/g, as determined by N_2 adsorption-desorption measurements (Fig. S3).

X-ray photoelectron spectroscopy (XPS) measurements were then performed to analyze the elemental composition and valence states. From the full spectra in Fig. 4a, the Bi, O, Br and Mo elements can be readily identified in all Mo-doped BiOBr samples, again, confirming successful doping of Mo into the BiOBr lattice (a similar profile was observed with undoped BiOBr except for the Mo peak) (B. Ma et al., 2021; J. Ma et al., 2021; Guo et al., 2019). From the high-resolution XPS scan of the Mo 3d electrons in 2%Mo-BiOBr (Fig. 4b), a doublet can be identified at 232.46 and 235.76 eV, corresponding to the Mo^{3+} $3d_{5/2}$ and $3d_{3/2}$ electrons (Y. Chen et al., 2021; X. Chen et al., 2021). Fig. 4c

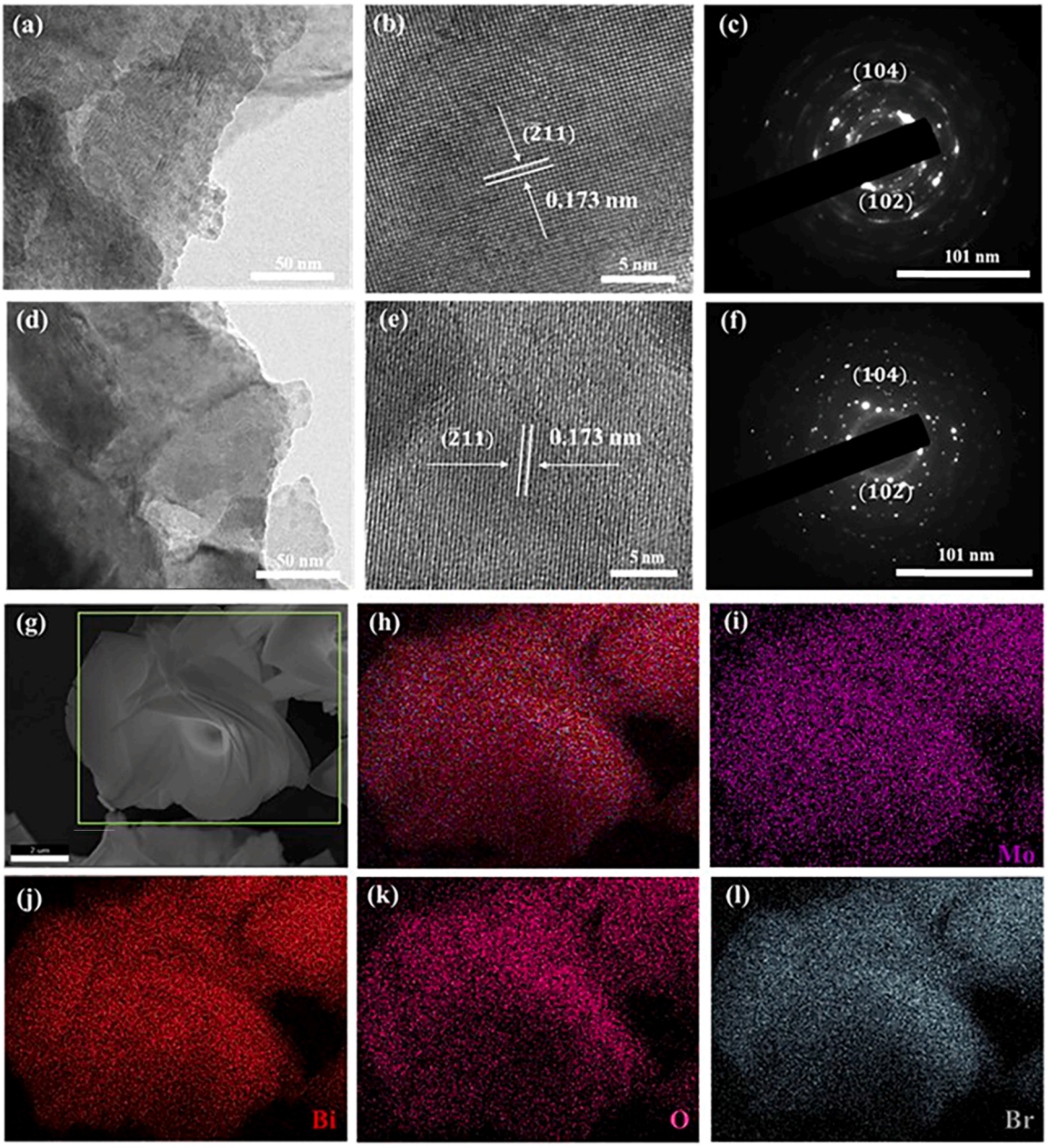

Fig. 3. (a,b,d,e) TEM and (c,f) SAED images of (a–c) undoped BiOBr and (d–f) 2%Mo-BiOBr. (g) SEM image and (h-l) the associated EDX elemental maps of 2%Mo-BiOBr: (i) Mo, (j) Bi, (k) O and (l) Br , with panel (h) showing the combined dirtcibution.

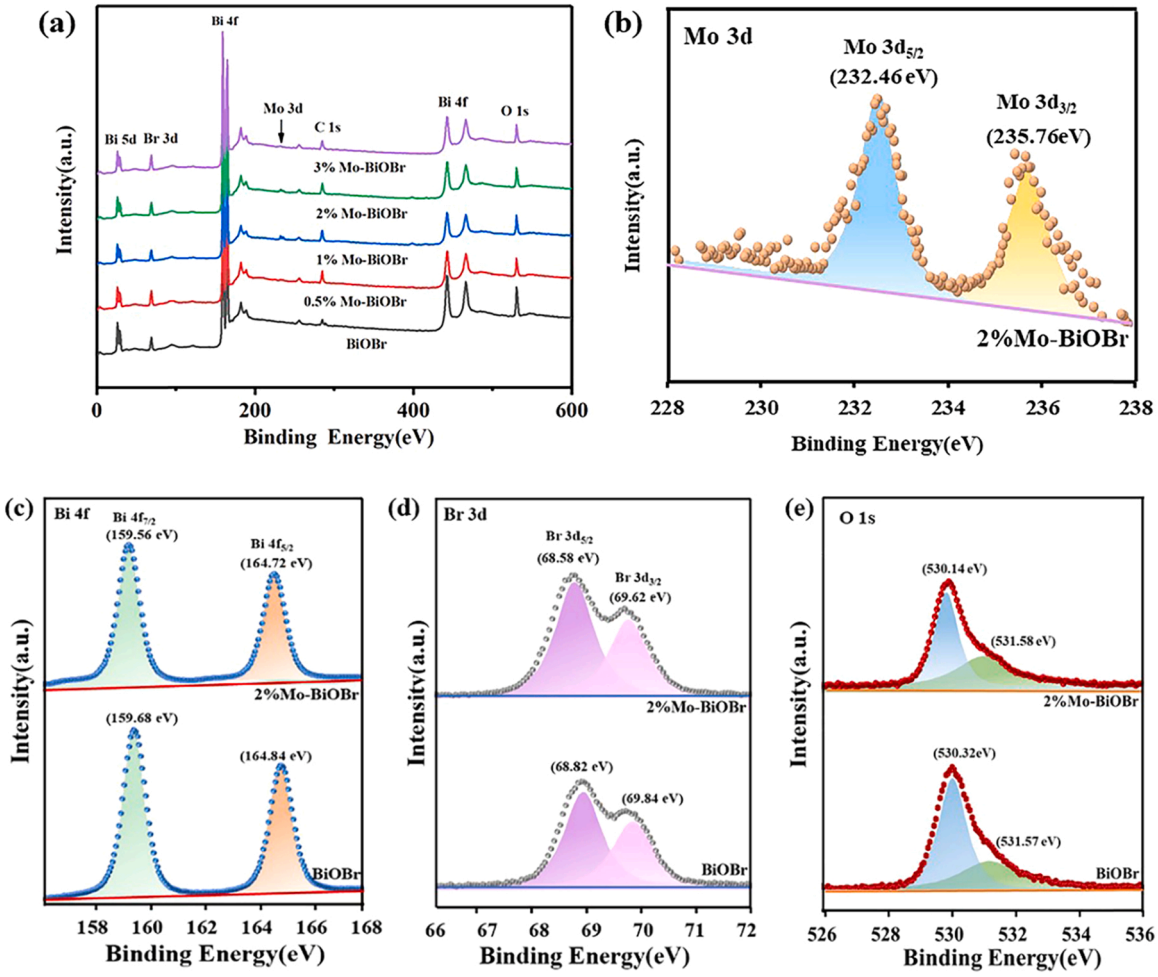

Fig. 4. (a) XPS survey spectra of pristine and Mo-doped BiOBr. (b) Mo 3d spectrum of 2%Mo-BiOBr. (c) Bi 4f, (d) Br 3d, and (e) O 1s spectra of BiOBr and 2%Mo-BiOBr. Dotted curves are experimental data and shaded peaks are deconvolution fits.

depicts the Bi 4f spectra of BiOBr and 2%Mo-BiOBr, both of which consisted of a doublet at 159.68/164.84 and 159.56/164.72 eV, respectively, due to the Bi^{3+} $4f_{7/2}$ and $4f_{5/2}$ electrons (X. Li et al., 2020; P. Li et al., 2020; Sun et al., 2021). The corresponding Br 3d spectra are shown in Fig. 4d. Again, both samples display a doublet at 68.82/69.84 and 68.58/69.62 eV, respectively, consistent with the Br^{-} $3d_{5/2}$ and $3d_{3/2}$ electrons (Shao et al., 2020). Fig. 4e depicts the O 1 s spectra, where two peaks can be deconvoluted for both samples, 530.32/531.57 eV for BiOBr, and 530.14/531.58 eV. The lower-energy peaks were due to the BiOBr lattice oxygen, whereas the higher-energy component arose from adsorbed hydroxyl groups on the material surface (H. Wang et al., 2021; C.Y. Wang et al., 2021; X. Wang et al., 2021). Notably, one can see that in comparison to undoped BiOBr, the binding energies of the Bi 4f, Br 3d, and lattice O 1s electrons all exhibited a clear diminishment in 2% Mo-BiOBr (X. Li et al., 2020; P. Li et al., 2020), suggesting that Mo doping led to electron enrichment in the BiOBr matrix (Huang et al., 2020; Lv et al., 2020).

3.2. Photo absorption and photoelectrochemical analysis

From the UV–vis diffuse reflectance spectroscopy (DRS) profiles in Fig. 5a, one can see that the absorption of undoped BiOBr is primarily limited to the UV/blue range ($\lambda < 450$ nm), whereas significantly enhanced absorption in the visible range can be seen with the Mo-doped BiOBr composites (Z. Sun et al., 2021; J. Sun et al., 2021). Among them, the 2%Mo-BiOBr sample showed the highest absorption across the entre range of 200–800 nm, a key feature that led to the best photocatalytic performance of sulfanilamide degradation (vide infra). This suggests dramatic impacts of Mo doping on the BiOBr electronic energy structure. More insights can be obtained from the corresponding Tauc plots depicted in the panel inset (Chen et al., 2020), $(\alpha h\nu)^{1/n} = A(h\nu - E_g)$, with α being the molar extinction coefficient, E_g the material band gap, ν photon frequency, h Planck's constant, and A constant coefficient. n is determined by the optical transition type (for indirect semiconductors like BiOBr, n = 4) (Tang et al., 2021). One can see that Mo doping led to an apparent diminishment of the BiOBr band gap, decreasing from 2.81 eV for undoped BiOBr to 2.59 eV for 0.5%Mo-BiOBr, 2.52 eV for 1%Mo-BiOBr, 2.13 eV for 2%Mo-BiOBr, and 2.26 eV for 3%Mo-BiOBr, consistent with the increased absorption in the visible range (Y. Chen et al., 2021; X. Chen et al., 2021). The is likely due to the formation of structural defects and additional band states (Shahid et al., 2020). Notably, the 2%Mo-BiOBr sample can be seen to exhibit the smallest bandgap among the series, corresponding to the best photocatalytic performance, as observed below (the fact that 3%Mo-BiOBr actually exhibited a slight increase of the bandgap was probably because of agglomeration of Mo dopants on the BiOBr surface, Huang et al., 2019).

To further explore the influence of Mo doping on the material energy structure, XPS valence band analysis was carried out to determine the valence band maximum (VBM). From Fig. 5b, the undoped BiOBr and 2%Mo-BiOBr can be seen to exhibit a VBM of 2.54 and 1.75 eV, respectively. In conjunction with the band gap determined from the above UV–vis DRS measurements (Fig. 5a), the conduction band minimum (CBM) was estimated to be − 0.27 eV for the undoped BiOBr and − 0.38 eV for 2%Mo-BiOBr. The corresponding band structures are

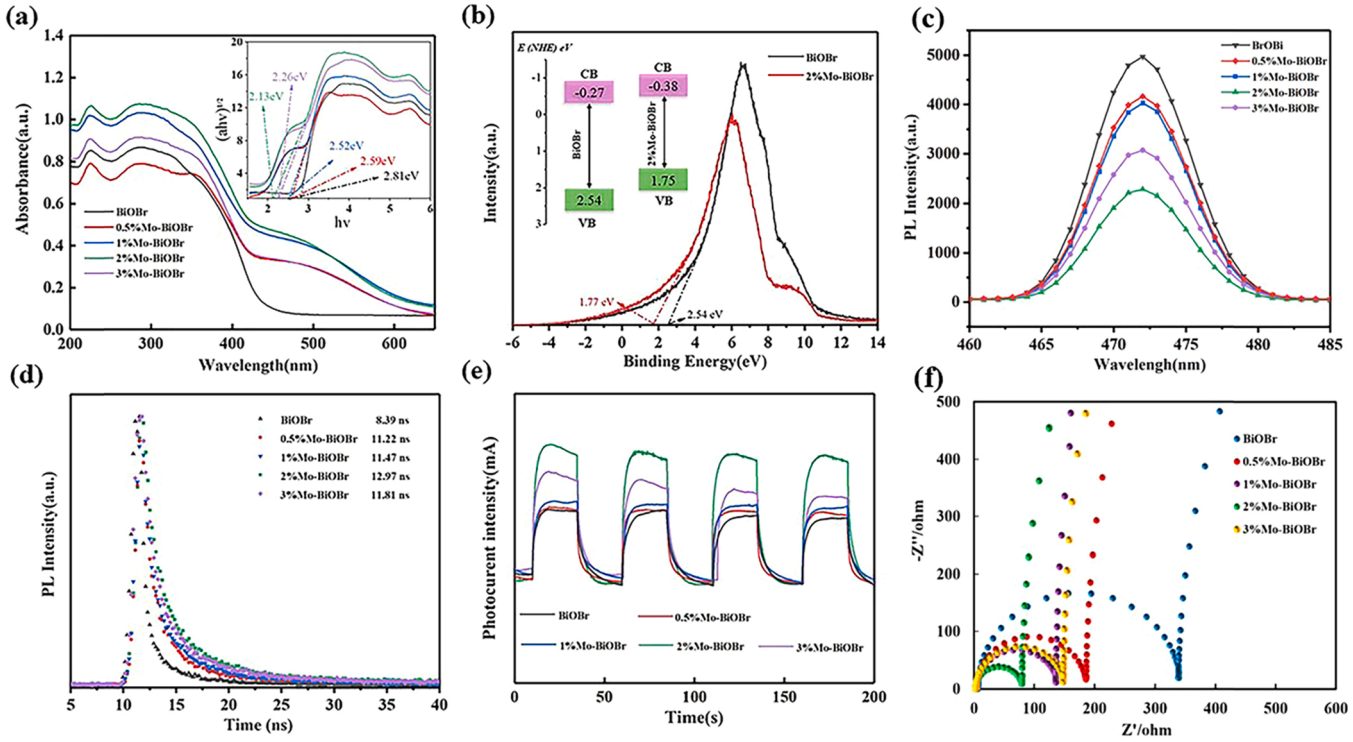

Fig. 5. (a) UV–vis DRS spectra of BiOBr and Mo-doped BiOBr. Inset is the corresponding Tauc plot. (b) VB XPS spectra of BiOBr and 2%Mo-BiOBr. Inset is the band structure. (c) Photoluminescence spectra, (d) time-resolved photoluminescence spectra, (e) transient photocurrent responses and (f) Nyquist plots of BiOBr and Mo-doped BiOBr.

shown in the inset to Fig. 5b.

The corresponding photoluminescence emission profiles are shown in Fig. 5c. At 310 nm excitation, the sample series can all be seen to display an emission centered at 472 nm, but the emission intensity varied in the order of BiOBr > 0.5%Mo-BiOBr > 1%Mo-BiOBr > 3% Mo-BiOBr > 2%Mo-BiOBr, suggesting that the recombination rate decreased with Mo doping and was the lowest with the 2%Mo-BiOBr sample, a characteristic conducive to charge separation and photocatalytic activity. Indeed, from time-resolved photoluminescence (TRPL) measurements (Fig. 5d), the average fluorescence lifetimes (τ_{ave}, Table S2) of BiOBr, 0.5%Mo-BiOBr, 1%Mo-BiOBr, 2%Mo-BiOBr, 3%Mo-BiOBr were estimated to be 8.39, 11.22, 11.42, 12.97 and 11.81 ns, respectively, suggesting that doping of Mo markedly boosted the efficiency of electron-hole separation, a unique feature for enhanced photocatalytic performance (X. Xu et al., 2021; J. Xu et al., 2021). Notably, 2% Mo-doped BiOBr exhibited a longer τ_{ave} than other samples in the series.

Consistent behaviors were observed in photocurrent measurements. From Fig. 5e, one can see that under visible light irradiation, the Mo-doped BiOBr samples all exhibited a higher photocurrent response than undoped BiOBr, and 2%Mo-BiOBr stood out with the highest photocurrents, again, suggesting most efficient electron-hole separation (Shang et al., 2021; Fu et al., 2021). The charge transfer properties were then investigated by electrochemical impedance spectroscopy (EIS) measurements. Curve fitting of the Nyquist plots in Fig. 5f with the Randles' equivalent circuit shows that the charge-transfer resistance (R_{CT}) was 337.9 Ω for undoped BiOBr, and decreased substantially to 185.4 Ω for 0.5%Mo-BiOBr, 135.5 Ω for 1%Mo-BiOBr, 79.1 Ω for 2% Mo-BiOBr, and 147.8 Ω for 3%Mo-BiOBr. The fact that the 2%Mo-BiOBr sample exhibited the lowest R_{CT} suggests the most efficient charge transfer (Guo et al., 2020), which was conducive to photo-induced carrier transport. Taken together, these results indicate that Mo doping led to a drastic change of the electronic energy structure of BiOBr, as manifested with a diminished bandgap, enhanced absorption in the visible range, improved separation of photogenerated electron-hole pairs, and reduced charge-transfer resistance (Fei et al., 2021). Consequently, marked enhancement of the photocatalytic activity was observed towards the degradation of sulfanilamide, as detailed below.

3.3. Photocatalytic performance

3.3.1. Sulfanilamide degradation

Sulfanilamide was used as the illustrating example to test the photocatalytic activity of the samples obtained above. Experimentally, a calculated amount of the undoped and Mo-doped BiOBr (0.3 g L^{-1}, Fig. S4) was dissolved in a 10 mg L^{-1} (Fig. S5) sulfanilamide solution at pH = 6.2 (Fig. S6). The solution was let undisturbed in the dark for 30 min to acquire an adsorption-desorption equilibrium, prior to the exposure to visible light illumination (Wang et al., 2019, 2018). From Fig. 6a, one can see that sulfanilamide exhibited virtually zero self-degradation in the absence of any photocatalyst; yet in the presence of BiOBr, apparent degradation occurred, and after visible photoirradiation for 80 min, the sulfanilamide concentration decreased by ca. 18.5%. The photocatalytic performance was further improved with the Mo-doped BiOBr samples, and 2%Mo-BiOBr emerged as the best catalyst among the series. For instance, after visible light illumination for 80 min, the remaining sulfanilamide concentration was only 48.3% for 0.5%Mo-BiOBr, 33.8% for 1%Mo-BiOBr, 12.5% for 2%Mo-BiOBr, and 20.1% for 3%Mo-BiOBr. This performance is highly comparable/superior to results of leading catalysts reported recently in the literature (Table S3). To examine the degree of photocatalytic mineralization of sulfanilamide, the total organic carbon concentration of the suspension before photoreaction (TOC_0) and after 80 min of visible light irradiation (TOC_e) were measured and compared. As shown in Fig. S7, the TOC_e/TOC_0 ratio varied in the order of 2%Mo-BiOBrb(0.65) < 3% Mo-BiOBr (0.69) < 1%Mo-BiOBr (0.86) < 0.5%Mo-BiOBr (0.92) < BiOBr (0.98), indicating effective mineralization of the sulfanilamide

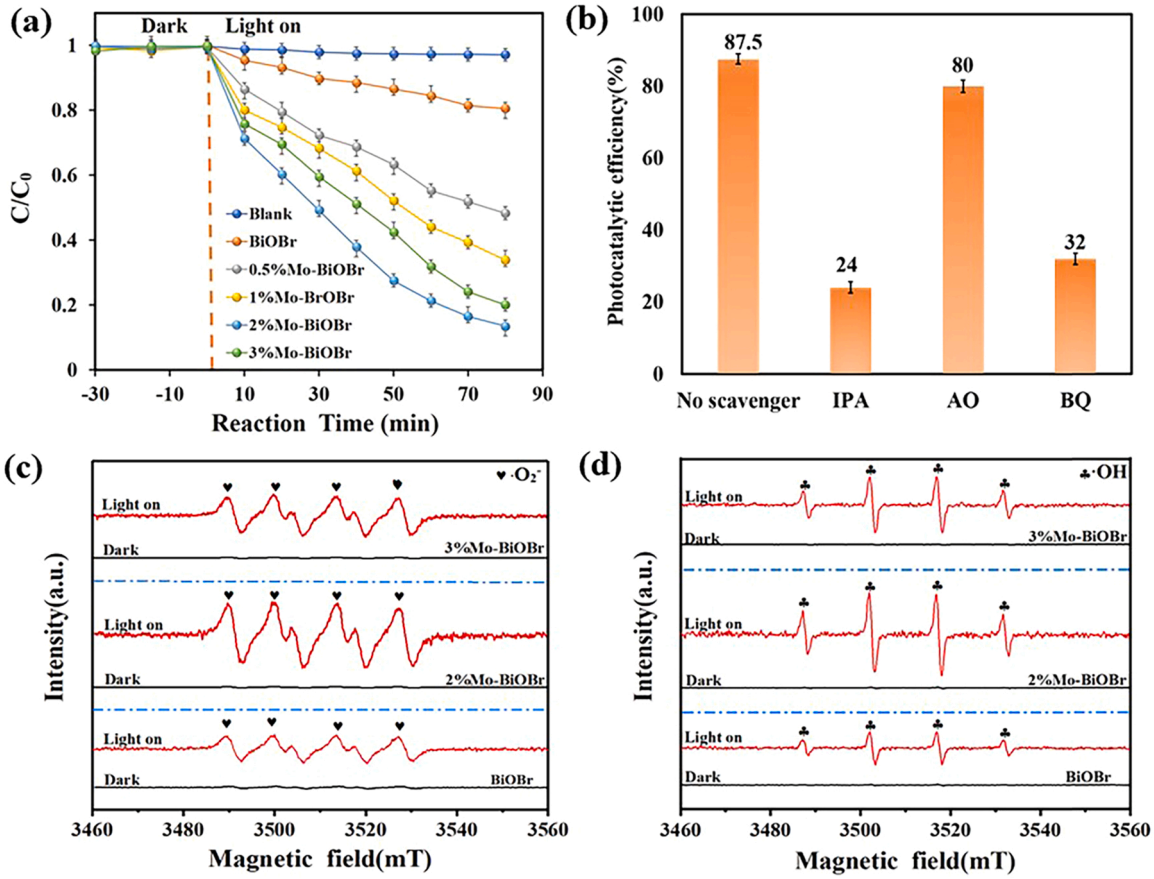

Fig. 6. (a) Degradation of sulfanilamide photocatalyzed by pristine and Mo-doped BiOBr. (b) Effect of scavengers on the degradation of sulfanilamide by 2%Mo-BiOBr. ESR spectra of (c) DMPO-$O_2^{\bullet-}$ (in H_2O) and (d) DMPO-•OH (in methanol) generated by different catalysts in the dark and under visible light irradiation.

molecules during the photocatalytic process, and the mineralization rate was the highest with 2%Mo-BiOBr.

Note that the undoped BiOBr exhibited a water contact angle of 41.2 ± 2° (Fig. S8a), which decreased drastically to 20 ± 2° for 2%Mo-BiOBr (Fig. S8b). This suggests that Mo doping significantly improved the hydrophilicity of the BiOBr surface, which may be due to the formation of hydrophilic oxygen-containing species on the sample surface after Mo-doping (S. Li et al., 2021; M. Li et al., 2021; W. Li et al., 2021). Such enhanced water wettability is conducive to the adsorption of sulfanilamide molecules, a critical first step in the photocatalytic degradation (J. Liu et al., 2019; W. Liu et al., 2019; Li et al., 2021).

3.3.2. Free radicals

To evaluate the contribution of free radicals to sulfanilamide degradation, ammonium oxalate (AO), isopropanol (IPA), and benzoquinone (BQ) (X. Xu et al., 2021; J. Xu et al., 2021; Di et al., 2019) were added to the solution as respective scavengers for holes (h^+), •OH, and $O_2^{\bullet-}$. From Fig. 6b, it can be seen that upon the addition of BQ and IPA, the efficiency of sulfanilamide degradation was reduced significantly by 55.5% and 63.5%, whereas no obvious inhibitory effect was observed with AO, suggesting that •OH and $O_2^{\bullet-}$ radicals played a crucial role in the catalytic reaction, while minimal contributions from h^+.

Consistent results were obtained in ESR measurements with DMPO as the radical trap. From Fig. 6c and d, one can see that in the dark, undoped and Mo-doped BiOBr exhibited only a featureless profile (Zhou et al., 2021), whereas two quartets can be readily identified upon visible light irradiation, with a 1:1:1:1 and 1:2:2:1 signal intensity ratio. These were consistent with the DMPO-$O_2^{\bullet-}$ and DMPO-·OH adducts (Yang et al., 2020; Li et al., 2021), respectively, indicating effective generation of $O_2^{\bullet-}$ and·OH radicals by the photocatalysts. It is worth noting that 2% Mo-BiOBr exhibited the greatest peak-to-peak amplitudes among the sample series, in coincidence with the highest photocatalytic activity, as manifested in Fig. 6a.

3.3.3. Influence of co-existing ions on sulfanilamide degradation

As actual water body may also contain a range of inorganic ions, their impacts on the photodegradation efficiency need to be examined. Experimentally, the Box-Behnken experimental design method was used to investigate the impacts of co-existing ions on the photocatalytic elimination of sulfanilamide (Yi et al., 2021). According to relevant literature, inorganic cations (e.g., K^+, Na^+, Ca^{2+} and Mg^{2+}) in water show little influence on the actual degradation reaction (Yi et al., 2021; Zhao et al., 2020). Thus, only inorganic anions, e.g., Cl^-, NO_3^-, SO_4^{2-} and $H_2PO_4^-$, were examined in the present study. Table S4 and S5 list the concentration variables of the different ions (4 factors) and the experimental results of sulfanilamide removal (29 runs). Analysis of variance based on the quadratic polynomial model demonstrated the relationship between the sulfanilamide removal efficiency and different ion concentration variables can be reflected in the following equation, Efficiency% = 79.58 + 0.33 A - 0.42B + 1.77 C - 0.26D + 1.46AB + 0.32AC + 0.15 CE + 0.59 BCE - 0.92BD + 2.7CD + 0.78A^2 - 1.26B^2 - 2.84 C^2 + 2.15D^2.

Table S6 lists the results of the detailed analysis of variance. The r^2 and $r^2_{adjusted}$ values were 0.9886 and 0.9773, respectively, confirming a significant correlation between the actual and theoretical values. Furthermore, on the basis of the F-value in Table S5, the effects of the four anions on sulfanilamide elimination can be identified as A (7.74), B (12.98), C (225.47), and D (4.85). It is evident that NO_3^- and SO_4^{2-} have the most significant effects on sulfanilamide removal, followed by Cl^- and $H_2PO_4^-$. The response surface diagrams are displayed in Fig. 7,

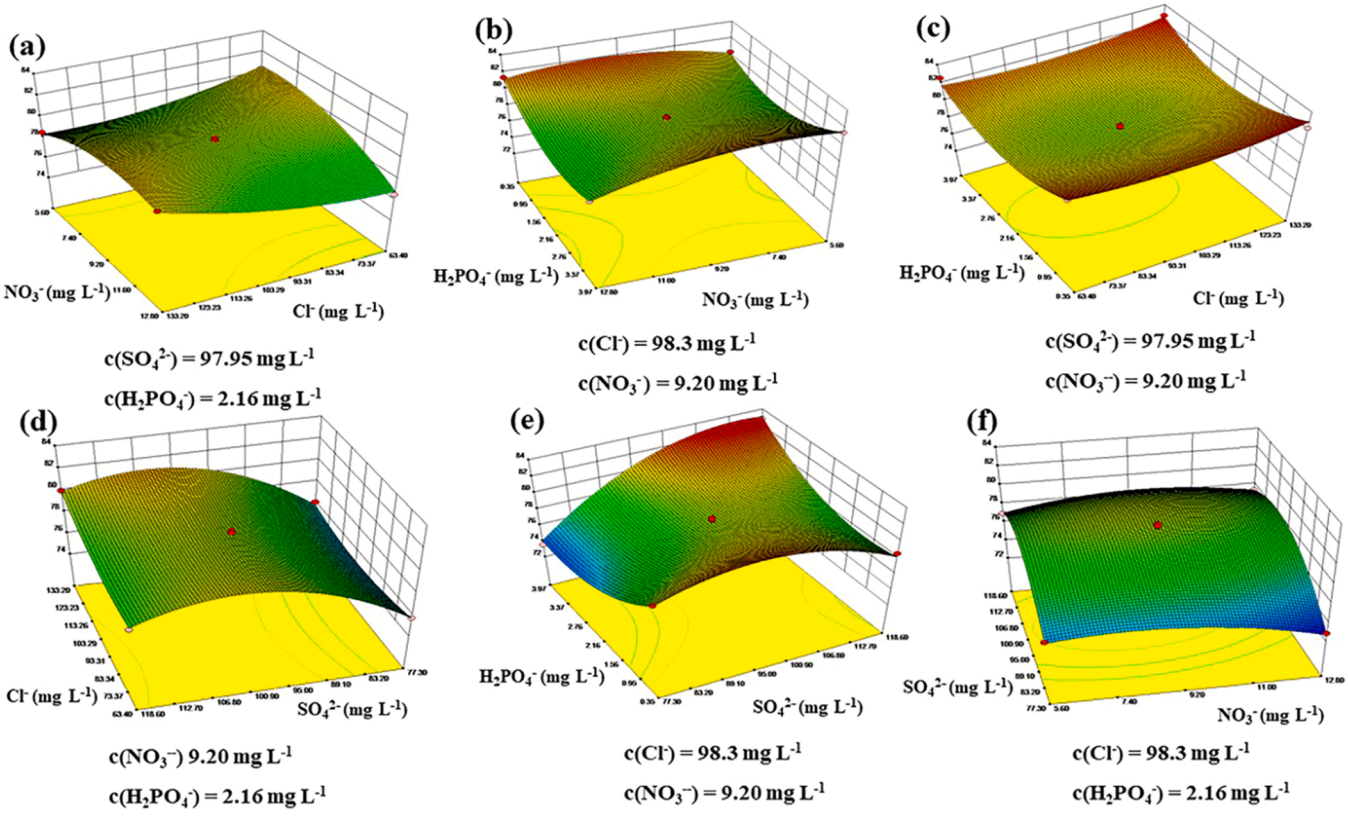

Fig. 7. Response surface plots of Cl^-, NO_3^-, SO_4^{2-} and $H_2PO_4^-$ concentrations on the photocatalytic degradation of sulfanilamide.

where SO_4^{2-} can be seen to show an inhibitory effect on sulfanilamide removal, while $H_2PO_4^-$ actually promoted the photocatalysis. Practically, to mitigate the negative effect of co-existing anions, one can appropriately increase the degradation time and/or increase the amount of catalysts.

4. Mechanism and reaction pathways of sulfanilamide degradation

As the photocatalytic degradation of sulfanilamide was primarily driven by radicals (Fig. 6), the active sites and regional selectivity of the sulfanilamide molecules were analyzed by theoretical calculations of the Fukui index (f^0, details in the Supplementary Information) (Ji et al., 2020). Fig. 8a and b show the chemical structure of sulfanilamide, and the associated lowest unoccupied molecular orbital (LUMO) and highest occupied molecular orbital (HOMO). In general, as the binding of electrons to HOMO is relatively weak, HOMO becomes easy to be attacked by free radicals (Wang et al., 2018). The Fukui index of electrophilic attack (f^+) and nucleophilic attack (f^-) to the sulfanilamide molecule was then calculated by natural population analysis (NPA) charge distribution (B. Li et al., 2019; H. Li et al., 2019; P. Li et al., 2019; Demircioglu et al., 2015; Dang et al., 2020; Pan et al., 2021), from which the possible attack sites by free radicals can be identified (Ji et al., 2021; Ma et al., 2021). From Fig. 8c, one can see that in the sulfanilamide molecule, the f^0 values of C1 (0.1158), C5 (0.1260) and N17 (0.1104) were markedly higher than others, suggesting that these were the atomic sites most likely attacked by free radicals.

LC-MS measurements were conducted to identify and examine the photocatalytic degradation intermediates (Fig. S9). In conjunction with results from DFT calculations, the photocatalytic degradation paths

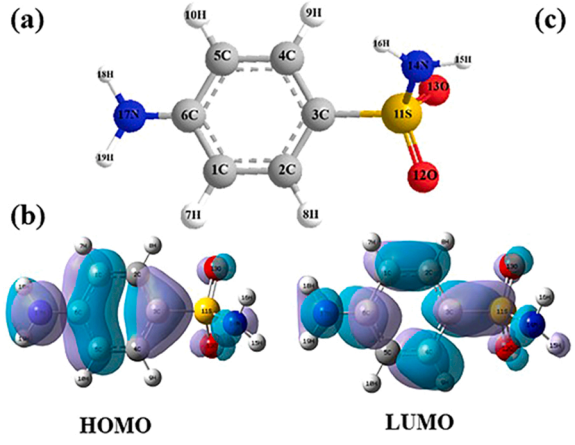

(c)

Atom	No	Charge (0)(e/Å^3)	Charge (+1)(e/Å^3)	Charge (-1)(e/Å^3)	f^-	f^+	f^0
C	1	-0.2862	-0.1922	-0.4238	0.0940	0.1375	0.1158
C	2	-0.1978	-0.1947	-0.3775	0.0031	0.1797	0.0914
C	3	-0.3752	-0.2229	-0.3662	0.1523	-0.0091	0.0716
C	4	-0.1890	-0.1818	-0.3188	0.0072	0.1298	0.0685
C	5	-0.2833	-0.2028	-0.4548	0.0805	0.1715	0.1260
C	6	0.1929	0.2296	0.2037	0.0368	-0.0108	0.0130
S	11	2.3340	2.3183	2.3311	-0.0157	0.0029	-0.0064
O	12	-0.9544	-0.8922	-0.9879	0.0622	0.0335	0.0478
O	13	-0.9566	-0.8942	-0.9869	0.0624	0.0303	0.0463
N	14	-1.1238	-1.0832	-1.1221	0.0406	-0.0017	0.0194
N	17	-0.8335	-0.6356	-0.8565	0.1979	0.0230	0.1104

Fig. 8. (a) Chemical structure, (b) HOMO and LUMO, and (c) NPA charge distribution and Fukui index of sulfanilamide.

were proposed in Fig. 9, which mainly entailed two pathways: (i) C3-S11 cleavage, and (ii) C6-N17 cleavage. Specifically, the attack of $O_2^{\bullet-}$ and·OH radicals led to the cleavages of the C-S and C-N bonds of sulfanilamide, forming unstable intermediates B ($m/z = 90.53$), C ($m/z = 130.16$), D ($m/z = 110.02$) and F ($m/z = 156.01$). Further attack of·OH resulted in the breaking of the phenyl rings of intermediates D and F generating E and G ($m/z = 113.96$), which were finally converted into H ($m/z = 102.03$). Intermediate H was ultimately decomposed into low-molecular-weight species, e.g., formic acid and oxalic acid, and mineralized into CO_2, H_2O and mineral acids (Yu et al., 2021; Feng et al., 2016).

On the basis of the test results presented above, the plausible mechanism of sulfanilamide degradation is shown in Fig. 10. The improved photocatalytic performance most likely arose from Mo doping and the dominant exposure of the (102) surface of the BiOBr nanosheets (Y. Chen et al., 2021; X. Chen et al., 2021; Li et al., 2019). Notably, Mo doping narrowed the BiOBr band gap, improved the utilization of visible light (J. Liu et al., 2019; W. Liu et al., 2019), promoted electron-hole separation and charge transfer (S. Li et al., 2021; M. Li et al., 2021; W. Li et al., 2021). In photocatalytic reaction, the e^- on the catalyst surface was excited to the conduction band (CB) from the valence band (VB), generating h^+ in the VB (Lv et al., 2020; Li et al., 2019), and the h^+ accumulated in the VB can directly oxidize the sulfanilamide molecules (Cui et al., 2021). Note that as the VBM of 2%Mo-BiOBr (1.75 eV) lies above the oxidation potential of H_2O to ·OH (2.38 eV vs NHE),·OH radicals were unlikely to be produced by h^+ oxidation of water (Cui et al., 2021). Instead, as the CBM (− 0.37 eV) of 2%Mo-BiOBr is more negative than the reduction potential of O_2 to $O_2^{\bullet-}$ (− 0.33 eV vs. NHE), the e^- on the catalyst surface can capture O_2 to form $O_2^{\bullet-}$, leading to the generation of·OH through a series of subsequent reactions ($e^- + O_2 \rightarrow O_2^{\bullet-}$, $O_2^{\bullet-} + 2\,H^+ \rightarrow H_2O_2$, $H_2O_2 + e^- \rightarrow \cdot OH + OH^-$). These free radicals then attacked the active sites of the sulfanilamide molecule, leading to the breaking of the chemical bonds, and finally effective degradation of the molecule (H. Wang et al., 2021; C.Y. Wang et al., 2021; X. Wang et al., 2021).

5. Catalyst reusability

The repeatability and stability of the catalysts represents another essential factor in the actual photocatalytic application. Fig. 11a shows the degradation of sulfanilamide by the same 2%Mo-BiOBr catalysts in 5 repeated cycles. One can see that the removal efficiency remained virtually unchanged (with a decrease < 2% after 5 cycles). Significantly, no obvious variation was observed in SEM (Fig. 11b), XRD and XPS measurements (Fig. 11c and d). This signifies the robust structure of the nanocomposite catalysts.

6. Conclusions

In summary, Mo-doped BiOBr nanocomposites were readily synthesized hydrothermally, which featured a three-dimensional lamellar structure, consistent with the undoped counterpart. Remarkably, the Mo-doped BiOBr exhibited a markedly enhanced performance in the photocatalytic elimination of sulfanilamide under visible light illumination, as compared to undoped BiOBr. This was ascribed to Mo doping that led to a significant change of the BiOBr electronic energy structure, as reflected in a narrowed bandgap, enhanced absorption in the visible range, improved electron-hole separation, as well as enhanced interfacial charge separation and transfer. With photogenerated free radicals responsible for the degradation activity, the Fukui index was calculated for the various atomic sites of the sulfanilamide molecule, from which the active sites for radical attacks were identified. The reaction pathways were finally proposed in conjunction with LC-MS measurements where the reaction intermediates and products were detected and analyzed. Results from this study suggest that structural engineering based on deliberate doping can serve as an effective strategy in the design of high-performance photocatalysts based on BiOBr.

CRediT authorship contribution statement

Yunyun Wu: Was responsible for the majority of the research work including data acquisition, analysis and organization, as well as initial paper drafting. **Haodong Ji:** Was responsible for the majority of the

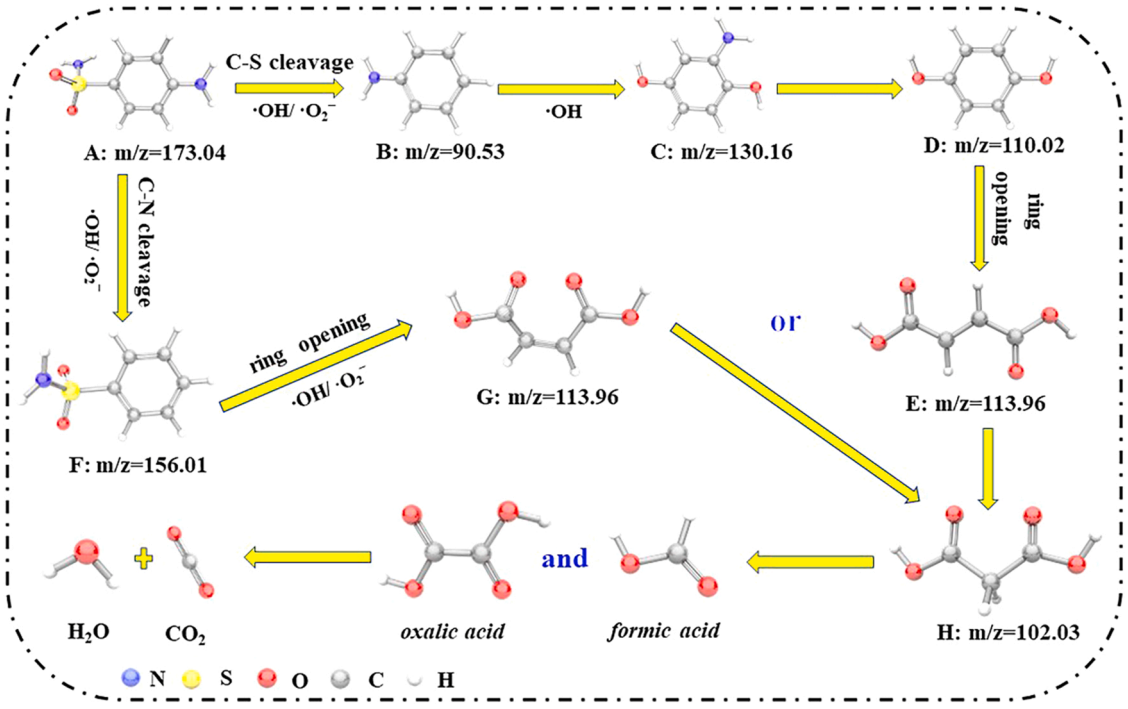

Fig. 9. Photocatalytic degradation pathways of sulfanilamide by Mo-doped BiOBr nanocomposites.

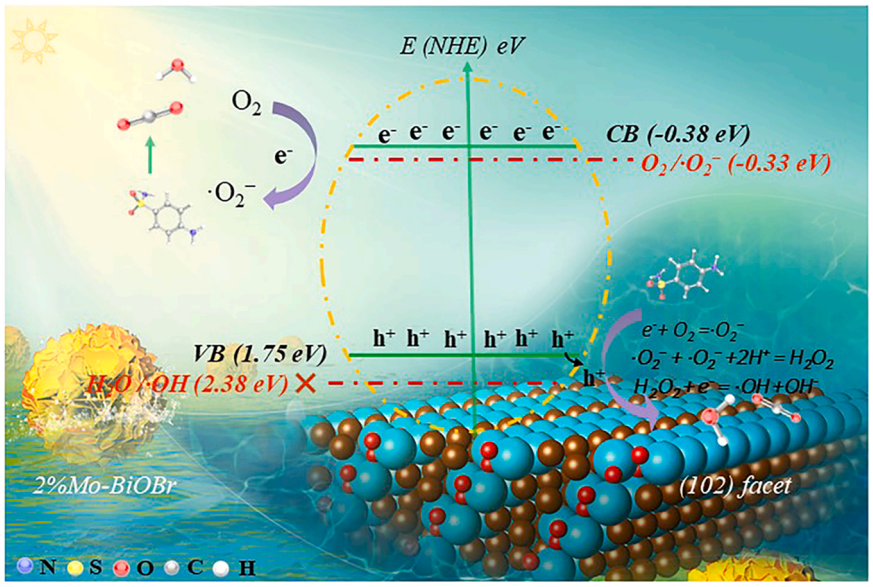

Fig. 10. Plausible mechanism of photocatalytic degradation of sulfanilamide by 2%Mo-BiOBr.

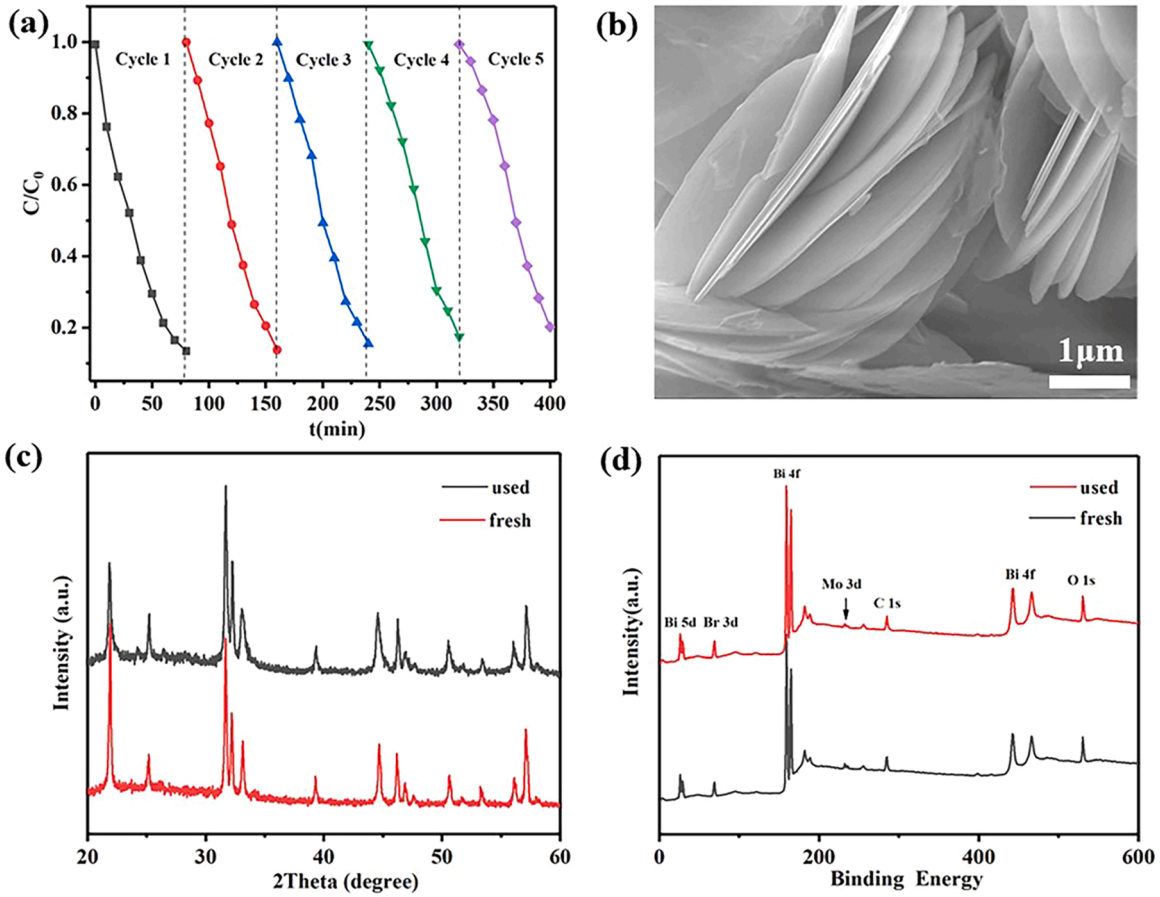

Fig. 11. (a) Photocatalytic degradation of sulfanilamide by 2%Mo-BiOBr in five consecutive runs. (b) SEM image, (c) XRD patterns and (d) XPS survey spectra of the catalysts after the photocatalytic tests.

research work including data acquisition, analysis and organization, as well as initial paper drafting. **Qiming Liu:** Assisted in data analysis and paper editing. **Zhaoyang Sun:** Assisted in data analysis and discussion. **Peisheng Li:** Assisted in data analysis and discussion. **Peiren Ding:** Assisted in data analysis and discussion. **Ming Guo:** Assisted in data analysis and discussion. **Xiaohong Yi:** Assisted in data analysis and discussion. **Wenlu Xu:** Assisted in data analysis and discussion. **Shuai Gao:** Assisted in data analysis and discussion. **Wen Liu:** Assisted in data analysis and discussion. **Chong-Chen Wang:** Supervised the project, provided resources and edited the paper. **Qiang Wang:** Supervised the

project, provided resources and edited the paper. **Shaowei Chen:** Finalized data analysis and paper editing.

Declaration of Competing Interest

The authors declare that they have no known competing financial interests or personal relationships that could have appeared to influence the work reported in this paper.

Acknowledgment

S.W.C. acknowledges partial support of the work by a grant from the National Science Foundation (CBET-1848841).

Appendix A. Supporting information

Supplementary data associated with this article can be found in the online version at doi:10.1016/j.jhazmat.2021.127563.

References

Adamek, E., Baran, W., Ziemiańska, J., Sobczak, A., 2012. Effect of FeCl3 on sulfonamide removal and reduction of antimicrobial activity of wastewater in a photocatalytic process with TiO2. Appl. Catal. B Environ. 126, 29–38.

Chen, M., Guo, C., Hou, S., Lv, J., Zhang, Y., Zhang, H., Xu, J., 2020. A novel Z-scheme AgBr/P-g-C3N4 heterojunction photocatalyst: excellent photocatalytic performance and photocatalytic mechanism for ephedrine degradation. Appl. Catal. B Environ. 266, 118614.

Chen, X., Zhang, X., Li, Y.H., Qi, M.Y., Li, J.Y., Tang, Z.R., Zhou, Z.Y., Xu, J., 2021. Transition metal doping BiOBr nanosheets with oxygen vacancy and exposed {102} facets for visible light nitrogen fixation. Appl. Catal. B Environ. 281, 119516.

Chen, Y., Tian, H., Zhu, W., Zhang, X., Li, R., Chen, C., Huang, Y., 2021. l-Cysteine directing synthesis of BiOBr nanosheets for efficient cefazolin photodegradation: the pivotal of thiol. J. Hazard. Mater. 414, 125544.

Cui, J., Tao, S., Yang, X., Yu, X., Sun, S., Yang, Q., Wei, W., Liang, S., 2021. Facile construction of nickel-doped hierarchical BiOCl architectures for enhanced visible-light-driven photocatalytic activities. Mater. Res. Bull. 138, 111208.

Dang, C., Sun, F., Jiang, H., Huang, T., Liu, W., Chen, X., Ji, H., 2020. Pre-accumulation and in-situ destruction of diclofenac by a photo-regenerable activated carbon fiber supported titanate nanotubes composite material: intermediates, DFT calculation, and ecotoxicity. J. Hazard. Mater. 400, 123225.

Demircioglu, Z., Kastas, C., Buyukgungor, O., 2015. Theoretical analysis (NBO, NPA, Mulliken Population Method) and molecular orbital studies (hardness, chemical potential, electrophilicity and Fukui function analysis) of (*E*)-2-((4-hydroxy-2-methylphenylimino)methyl)-3-methoxyphenol. J. Mol. Struct. 1091, 183–195.

Di, G., Zhu, Z., Zhang, H., Zhu, J., Qiu, Y., Yin, D., Kuppers, S., 2019. Visible-light degradation of sulfonamides by Z-scheme ZnO/g-C3N4 heterojunctions with amorphous Fe2O3 as electron mediator. J. Colloid Interface Sci. 538, 256–266.

Dong, S., Pi, Y., Li, Q., Hu, L., Li, Y., Han, X., Wang, J., Sun, J., 2016. Solar photocatalytic degradation of sulfanilamide by BiOCl/reduced graphene oxide nanocomposites: mechanism and degradation pathways. J. Alloy. Compd. 663, 1–9.

Du, J., Xiao, G., Xi, Y., Zhu, X., Su, F., Kim, S.H., 2020. Periodate activation with manganese oxides for sulfanilamide degradation. Water Res. 169, 115278.

Fei, H., Shao, J., Li, H., Li, N., Chen, D., Xu, Q., He, J., Lu, J., 2021. Construction of ultra-thin 2D CN-Br0.12/2%RhOx photo-catalyst with rapid electron and hole separation for efficient bisphenol A degradation. Appl. Catal. B Environ. 299, 120623.

Feng, Y., Liao, C., Shih, K., 2016. Copper-promoted circumneutral activation of H2O2 by magnetic CuFe2O4 spinel nanoparticles: mechanism, stoichiometric efficiency, and pathway of degrading sulfanilamide. Chemosphere 154, 573–582.

Fu, S., Zhu, H., Huang, Q., Liu, X., Zhang, X., Zhou, J., 2021. Construction of hierarchical CuBi2O4/Bi/BiOBr ternary heterojunction with Z-scheme mechanism for enhanced broad-spectrum photocatalytic activity. J. Alloy. Compd. 878, 160372.

Ghahremani, H., 2017. Photocatalytic degradation of antibacterial sulfanilamide from aqueous solution using TiO2 nanocatalyst. J. Nano Res. 46, 111–122.

Guo, F., Chen, J., Zhao, J., Chen, Z., Xia, D., Zhan, Z., Wang, Q., 2020. Z-scheme heterojunction g-C3N4@PDA/BiOBr with biomimetic polydopamine as electron transfer mediators for enhanced visible-light driven degradation of sulfamethoxazole. Chem. Eng. J. 386, 124014.

Guo, J., Liao, X., Lee, M.H., Hyett, G., Huang, C.C., Hewak, D.W., Mailis, S., Zhou, W., Jiang, Z., 2019. Experimental and DFT insights of the Zn-doping effects on the visible-light photocatalytic water splitting and dye decomposition over Zn-doped BiOBr photocatalysts. Appl. Catal. B Environ. 243502–243512.

Gupta, G., Kaur, A., Sinha, A.S.K., Kansal, S.K., 2017. Photocatalytic degradation of levofloxacin in aqueous phase using Ag/AgBr/BiOBr microplates under visible light. Mater. Res. Bull. 88, 148–155.

Hamiwe, T., Kock, M.M., Magwira, C.A., Antiabong, J.F., Ehlers, M.M., 2019. Occurrence of enterococci harbouring clinically important antibiotic resistance genes in the aquatic environment in Gauteng, South Africa. Environ. Pollut. 245, 1041–1049.

Han, J., Zhu, Z., Li, N., Chen, D., Xu, Q., Li, H., He, J., Lu, J., 2021. Metalloporphyrin-based D-A type conjugated organic polymer nanotube for efficient photocatalytic degradation. Appl. Catal. B Environ. 291, 120108.

Huang, M., Li, J., Su, W., Huang, X., Li, B., Fan, M., Dong, L., He, H., 2020. Oriented construction of S-doped, exposed {001} facet BiOBr nanosheets with abundant oxygen vacancies and promoted visible-light-driven photocatalytic performance. CrystEngComm 22, 7684–7692.

Huang, Y., Xu, H., Luo, D., Zhao, Y., Fang, Y., Wei, Y., Fan, L., Wu, J., 2019. Facile in situ synthesis of Ag and Bi co-decorated BiOCl heterojunction with high photocatalytic performance over the full solar spectrum. Solid State Sci. 89, 74–84.

Hunge, Y., Yadav, A., Kang, S., Kim, H., 2021a. Photocatalytic degradation of tetracycline antibiotics usinghydrothermally synthesized two-dimensional molybdenum disulfide/titanium dioxide composites. J. Colloid Interface Sci. 606, 454–463.

Ji, H., Du, P., Zhao, D., Li, S., Sun, F., Duin, E.C., Liu, W., 2020. 2D/1D graphitic carbon nitride/titanate nanotubes heterostructure for efficient photocatalysis of sulfamethazine under solar light: catalytic "hot spots" at the rutile–anatase–titanate interfaces. Appl. Catal. B Environ. 263, 118357.

Ji, H., Liu, W., Sun, F., Huang, T., Chen, L., Liu, Y., Qi, J., Xie, C., Zhao, D., 2021. Experimental evidences and theoretical calculations on phenanthrene degradation in a solar-light-driven photocatalysis system using silica aerogel supported TiO2 nanoparticles: insights into reactive sites and energy evolution. Chem. Eng. J. 419, 129605.

Jiao, W., Xie, Y., He, F., Wang, K., Ling, Y., Hu, Y., Wang, J., Ye, H., Wu, J., Hou, Y., 2021. A visible light-response flower-like La-doped BiOBr nanosheets with enhanced performance for photoreducing CO_2 to CH3OH. Chem. Eng. J. 418, 129286.

Khan, F.S.A., Mubarak, M.N., Tan, Y.H., Khalid, M., Karri, R.R., Walvekar, R., Abdullah, E.C., Nizamuddin, S., Mazari, S.A., 2021. A comprehensive review on magnetic carbon nanotubes and carbon nanotube-based buckypaper for removal of heavy metals and dyes. J. Hazard. Mater. 413, 125375.

Li, B., Lai, C., Xu, P., Zeng, G., Huang, D., Qin, L., Yi, H., Cheng, M., Wang, L., Huang, F., Liu, S., Zhang, M., 2019. Facile synthesis of bismuth oxyhalogen-based Z-scheme photocatalyst for visible-light-driven pollutant removal: kinetics, degradation pathways and mechanism. J. Clean. Prod. 225, 898–912.

Li, H., Deng, F., Zheng, Y., Hua, L., Qu, C., Luo, X., 2019. Visible-light-driven Z-scheme rGO/Bi2S3–BiOBr heterojunctions with tunable exposed BiOBr (102) facets for efficient synchronous photocatalytic degradation of 2-nitrophenol and Cr(vi) reduction. Environ. Sci. Nano 6, 3670–3683.

Li, M., Wang, P., Ji, Z., Zhou, Z., Xia, Y., Li, Y., Zhan, S., 2021. Efficient photocatalytic oxygen activation by oxygen-vacancy-rich CeO2-based heterojunctions: synergistic effect of photoexcited electrons transfer and oxygen chemisorption. Appl. Catal. B Environ. 289, 120020.

Li, P., Guo, M., Wang, Q., Li, Z., Wang, C., Chen, N., Wang, C.C., Wan, C., Chen, S., 2019. Controllable synthesis of cerium zirconium oxide nanocomposites and their application for photocatalytic degradation of sulfonamides. Appl. Catal. B Environ. 259, 118107.

Li, P., Zhou, Z., Wang, Q., Guo, M., Chen, S., Low, J., Long, R., Liu, W., Ding, P., Wu, Y., Xiong, Y., 2020. Visible-light-driven nitrogen fixation catalyzed by Bi5O7Br nanostructures: enhanced performance by oxygen vacancies. J. Am. Chem. Soc. 142, 12430–12439.

Li, S., Wang, C., Liu, Y., Xue, B., Jiang, W., Liu, Y., Mo, L., Chen, X., 2021. Photocatalytic degradation of antibiotics using a novel Ag/Ag2S/Bi2MoO6 plasmonic p-n heterojunction photocatalyst: mineralization activity, degradation pathways and boosted charge separation mechanism. Chem. Eng. J. 415, 128991.

Li, W., Jin, L., Gao, F., Wan, H., Pu, Y., Wei, X., Chen, C., Zou, W., Zhu, C., Dong, L., 2021. Advantageous roles of phosphate decorated octahedral CeO2 {111}/g-C3N4 in boosting photocatalytic CO_2 reduction: charge transfer bridge and Lewis basic site. Appl. Catal. B Environ. 294, 120257.

Li, X., Wang, T., Tao, X., Qiu, G., Li, C., Li, B., 2020. Interfacial synergy of Pd sites and defective BiOBr for promoting the solar-driven selective oxidation of toluene. J. Mater. Chem. A. 8, 17657–17669.

Liu, G., Wang, H., Chen, D., Dai, C., Zhang, Z., Feng, Y., 2020. Photodegradation performances and transformation mechanism of sulfamethoxazole with CeO2/CN heterojunction as photocatalyst. Sep. Purif. Technol. 237, 116329.

Liu, J., Li, R., Zu, X., Zhang, X., Wang, Y., Wang, Y., Fan, C., 2019. Photocatalytic conversion of nitrogen to ammonia with water on triphase interfaces of hydrophilic-hydrophobic composite Bi4O5Br2/ZIF-8. Chem. Eng. J. 371, 796–803.

Liu, W., Li, Y., Liu, F., Jiang, W., Zhang, D., Liang, J., 2019. Visible-light-driven photocatalytic degradation of diclofenac by carbon quantum dots modified porous g-C3N4: mechanisms, degradation pathway and DFT calculation. Water Res. 151, 9–19.

Liu, Y., Zhang, X., Deng, J., Liu, Y., 2021. A novel CNTs-Fe3O4 synthetized via a ball-milling strategy as efficient fenton-like catalyst for degradation of sulfonamides. Chemosphere 277, 130305.

Lv, X., Yan, Y.S., Lam, F.L., Ng, Y.H., Yin, S., An, A.K., 2020. Solvothermal synthesis of copper-doped BiOBr microflowers with enhanced adsorption and visible-light driven photocatalytic degradation of norfloxacin. Chem. Eng. J. 401, 126012.

Ma, B., Xin, S., Xin, Y., Ma, X., Zhang, C., Gao, M., Ma, F., Ma, Y., 2021. Visible-light-driven photoelectrocatalytic degradation of p-chloronitrobenzene by BiOBr/TiO2 nanotube arrays photoelectrodes: mechanisms, degradation pathway and DFT calculation. Sep. Purif. Technol. 268, 118699.

Ma, J., Chen, L., Liu, Y., Xu, T., Ji, H., Duan, J., Sun, F., Liu, W., 2021. Oxygen defective titanate nanotubes induced by iron deposition for enhanced peroxymonosulfate activation and acetaminophen degradation: mechanisms, water chemistry effects, and theoretical calculation. J. Hazard. Mater. 418, 126180.

Niu, Z.L., Yi, S.S., Li, C.Q., Liu, Y., Pang, Q.Q., Liu, Z.Y., Yue, X.Z., 2020. Supporting bimetallic sulfide on 3D TiO2 hollow shells to boost photocatalytic activity. Chem. Eng. J. 390, 124602.

Pan, F., Ji, H., Du, P., Huang, T., Wang, C., Liu, W., 2021. Insights into catalytic activation of peroxymonosulfate for carbamazepine degradation by MnO2 nanoparticles in-situ anchored titanate nanotubes: mechanism, ecotoxicity and DFT study. J. Hazard. Mater. 402, 123779.

Qiao, X., Xu, Y., Yang, K., Ma, J., Li, C., Wang, H., Jia, L., 2020. Mo doped BiVO4 gas sensor with high sensitivity and selectivity towards H2S. Chem. Eng. J. 395, 125144.

Qin, K., Zhao, Q., Yu, H., Xia, X., Li, J., He, S., Wei, L., An, T., 2021b. A review of bismuth-based photocatalysts for antibiotic degradation: insight into the photocatalytic degradation performance, pathways and relevant mechanisms. Environ. Res. 199, 111360.

Qu, J., Du, Y., Ji, P., Li, Z., Jiang, N., Sun, X., Xue, L., Li, H., Sun, G., 2021. Fe, Cu co-doped BiOBr with improved photocatalytic ability of pollutants degradation. J. Alloy. Compd. 881, 160391.

Sadjid, M., Amin, N., Shad, N., Khan, S., Javed, Y., Zhang, Z., 2019. Hydrothermal fabrication of monoclinic bismuth vanadate (m-BiVO4) nanoparticles for photocatalytic degradation of toxic organic dyes. Mater. Sci. Eng. B 242, 83–89.

Senasu, T., Chankhanittha, T., Hemavibool, K., Nanan, S., 2021a. Solvothermal synthesis of BiOBr photocatalyst with an assistant of PVP for visible-light-driven photocatalytic degradation of fluoroquinolone antibiotics. Catal. Today. https://doi.org/10.1016/j.cattod.2021.04.008.

Senasu, T., Nijpanich, S., Juabrum, S., Chanlek, N., Nanan, S., 2021b. CdS/BiOBr heterojunction photocatalyst with high performance for solar-light-driven degradation of ciprofloxacin and norfloxacin antibiotics. Appl. Surf. Sci. 567, 150850.

Shahid, M., Mehmood, R., Athar, M., Hussain, J., Wei, Y., Khaliq, A., 2020. BiOCl Nanoplates doped with Fe3+ ions for the visible-light degradation of aqueous pollutants. ACS Appl. Nano Mater. 433, 746–758.

Shang, Y., Wang, T., Xiao, Y., Dong, Z., Li, X., Li, B., 2021. Constructing BiOBr/CoOx/g-C3N4 Z-scheme photocatalyst with CoOx as both redox mediator and cocatalyst for phenol degradation. J. Alloy. Compd. 875, 159998.

Shao, L., Liu, Y., Wang, L., Xia, X., Shen, X., 2020. Electronic structure tailoring of BiOBr (0 1 0) nanosheets by cobalt doping for enhanced visible-light photocatalytic activity. Appl. Surf. Sci. 502, 143895.

Sun, J., Li, X., Zhao, Q., Liu, B., 2021. Ultrathin nanoflake-assembled hierarchical BiOBr microflower with highly exposed {001} facets for efficient photocatalytic degradation of gaseous ortho-dichlorobenzene. Appl. Catal. B Environ. 281, 119478.

Sun, Z., Yang, X., Yu, X.F., Xia, L., Peng, Y., Li, Z., Zhang, Y., Cheng, J., Zhang, K., Yu, J., 2021. Surface oxygen vacancies of Pd/Bi2MoO6-x acts as "Electron Bridge" to promote photocatalytic selective oxidation of alcohol. Appl. Catal. B Environ. 285, 119790.

Tang, Q.Y., Yang, M.J., Yang, S.Y., Xu, Y.H., 2021. Enhanced photocatalytic degradation of glyphosate over 2D CoS/BiOBr heterojunctions under visible light irradiation. J. Hazard. Mater. 407, 124798.

Tayebi, M., Tayyebi, A., Lee, B., 2019. Improved photoelectrochemical performance of molybdenum (Mo)-doped monoclinic bismuth vanadate with increasing donor concentration. Catal. Today 328, 35–42.

Wang, C.Y., Zeng, Q., Zhu, G., 2021. Novel S-doped BiOBr nanosheets for the enhanced photocatalytic degradation of bisphenol A under visible light irradiation. Chemosphere 268, 128854.

Wang, F., Feng, Y., Chen, P., Wang, Y., Su, Y., Zhang, Q., Zeng, Y., Xie, Z., Liu, H., Liu, Y., Lv, W., Liu, G., 2018. Photocatalytic degradation of fluoroquinolone antibiotics using ordered mesoporous g-C3N4 under simulated sunlight irradiation: kinetics, mechanism, and antibacterial activity elimination. Appl. Catal. B Environ. 227, 114–122.

Wang, H., Cai, X., Zhang, Y., Zhang, T., Chen, M., Hu, H., Huang, Z., Liang, J., Qin, Y., 2021. Double-template-regulated bionic mineralization for the preparation of flower like BiOBr/carbon foam/PVP composite with enhanced stability and visible-light-driven catalytic activity. Appl. Surf. Sci. 555, 149708.

Wang, J., Zhuan, R., 2020. Degradation of antibiotics by advanced oxidation processes: an overview. Sci. Total Environ. 701, 135023.

Wang, J., Cui, C., Li, Y., Liu, Y., Zhang, Y., Shi, W., 2017. Porous Mn doped g-C3N4 photocatalysts for enhanced synergetic degradation under visible-light illumination. J. Hazard. Mater. 339, 43–53.

Wang, R., Tang, J., Zhang, X., Wang, D., Wang, X., Xue, S., Zhang, Z., Dionysiou, D.D., 2019. Construction of novel Z-scheme Ag/ZnFe2O4/Ag/BiTa1-xVxO4 system with enhanced electron transfer capacity for visible light photocatalytic degradation of sulfanilamide. J. Hazard. Mater. 375, 161–173.

Wang, X., Xu, G., Tu, Y., Wu, D., Li, A., Xie, X., 2021. BiOBr/PBCD-B-D dual-function catalyst with oxygen vacancies for Acid Orange 7 removal: evaluation of adsorption-photocatalysis performance and synergy mechanism. Chem. Eng. J. 411, 128456.

Wang, Y., Liu, X., Zhang, L., 2020. Assembling 3D hierarchical hollow flower-like Ni@N-doped graphitic carbon for boosting simultaneously efficient removal and sensitive monitoring of multiple sulfonamides. J. Hazard. Mater. 386, 121629.

Wu, D., Yue, S., Wang, W., An, T., Li, G., Yip, H.Y., Zhao, H., Wong, P.K., 2016. Boron doped BiOBr nanosheets with enhanced photocatalytic inactivation of Escherichia coli. Appl. Catal. B Environ. 192, 35–45.

Wu, J., Xie, Y., Ling, Y., Si, J., Li, X., Wang, J., Ye, H., Zhao, J., Li, S., Zhao, Q., Hou, Y., 2020. One-step synthesis and Gd3+ decoration of BiOBr microspheres consisting of nanosheets toward improving photocatalytic reduction of CO_2 into hydrocarbon fuel. Chem. Eng. J. 400, 125944.

Xu, J., Gao, Q., Wang, Z., Zhu, Y., 2021. An all-organic 0D/2D supramolecular porphyrin/g-C3N4 heterojunction assembled via π-π interaction for efficient visible photocatalytic oxidation. Appl. Catal. B Environ. 291, 120059.

Xu, X., Meng, L., Luo, J., Zhang, M., Wang, Y., Dai, Y., Sun, C., Wang, Z., Yang, S., He, H., Wang, S., 2021. Self-assembled ultrathin CoO/Bi quantum dots/defective Bi2MoO6 hollow Z-scheme heterojunction for visible light-driven degradation of diazinon in water matrix: intermediate toxicity and photocatalytic mechanism. Appl. Catal. B Environ. 293, 120231.

Yan, P., Xu, L., Jiang, D., Li, H., Xia, J., Zhang, Q., Hua, M., Li, H., 2018. Photoelectrochemical monitoring of ciprofloxacin based on metallic Bi self-doping BiOBr nanocomposites. Electrochim. Acta 259, 873–881.

Yang, Y., Zeng, G., Huang, D., Zhang, C., He, D., Zhou, C., Wang, W., Xiong, W., Li, X., Li, B., Dong, W., Zhou, Y., 2020. Molecular engineering of polymeric carbon nitride for highly efficient photocatalytic oxytetracycline degradation and H2O2 production. Appl. Catal. B Environ. 272, 118970.

Yi, X.H., Ji, H., Wang, C.C., Li, Y., Li, Y.H., Zhao, C., Wang, A., Fu, H., Wang, P., Zhao, X., Liu, W., 2021. Photocatalysis-activated SR-AOP over PDINH/MIL-88A(Fe) composites for boosted chloroquine phosphate degradation: performance, mechanism, pathway and DFT calculations. Appl. Catal. B Environ. 293, 120229.

Younis, M.A., Lyu, S., Lei, C., Yang, B., Li, Z., He, Q., Lu, J., Lei, L., Hou, Y., 2021. Efficient mineralization of sulfanilamide over oxygen vacancy-rich NiFe-LDH nanosheets array during electro-fenton process. Chemosphere 268, 129272.

Yu, H., Liu, G., Dong, B., Jin, R., Zhou, J., 2021. Synergistic catalytic Fenton-like degradation of sulfanilamide by biosynthesized goethite-reduced graphene oxide composite. J. Hazard. Mater. 415, 125704.

Zhang, H., Yang, Y., Zhou, Z., Zhao, Y., Liu, L., 2014. Enhanced photocatalytic properties in BiOBr nanosheets with dominantly exposed (102) facets. J. Phys. Chem. C 118, 14662–14669.

Zhao, C., Wang, Z., Li, X., Yi, X., Chu, H., Chen, X., Wang, C.C., 2020. Facile fabrication of BUC-21/Bi24O31Br10 composites for enhanced photocatalytic Cr(VI) reduction under white light. Chem. Eng. J. 389, 123431.

Zhou, L., Dai, S., Xu, S., She, Y., Li, Y., Leveneur, S., Qin, Y., 2021. Piezoelectric effect synergistically enhances the performance of Ti32-oxo-cluster/BaTiO3/CuS p-n heterojunction photocatalytic degradation of pollutants. Appl. Catal. B Environ. 291, 120019.

Zhu, W., Liu, J., Yu, S., Zhou, Y., Yan, X., 2016. Ag loaded WO3 nanoplates for efficient photocatalytic degradation of sulfanilamide and their bactericidal effect under visible light irradiation. J. Hazard. Mater. 318, 407–416.